Influence of Blood Rheology and Outflow Boundary Conditions in Numerical Simulations of Cerebral Aneurysms

Susana Ramalho, Alexandra B. Moura, Alberto M. Gambaruto, and Adélia Sequeira

1 Introduction

Disease in human physiology is often related to cardiovascular mechanics. Impressively, strokes are one of the leading causes of death in developed countries, and they might occur as a result of an aneurysm rupture, which is a sudden event in the majority of cases. On the basis of several autopsy and angiography series, it is estimated that 0.4–6 % of the general population harbors one or more intracranial aneurysms, and on average the incidence of an aneurysmal rupture is of 10 per 100,000 population per year, with tendency to increase in patients with multiple aneurysms [14, 20].

An aneurysm is a localized pathological dilation of the wall of a blood vessel, due to the congenital or acquired structural weakening of the wall media, and potentially results in severe complications, or even sudden death, through pressing on adjacent structures, or rupturing causing massive hemorrhage [10]. They are primarily located in different segments of the aorta and in the intracranial arteries supplying the brain. Moreover, intracranial aneurysms are most likely to be encountered on or close to the circle of Willis, particularly in apices of the bifurcation of first- and second-order arteries, and in curved arterial segments [28]. The natural history of this pathology is far from being fully understood, which can be related to the paucity of temporal investigations, since aneurysms are rarely detected before rupture. It is believed that the formation, growth, and rupture of intracranial aneurysms are associated with local hemodynamics, other than lumen structural mechanics and biomedical responses.

S. Ramalho • A.B. Moura • A.M. Gambaruto • A. Sequeira (✉)
Department of Mathematics and CEMAT, Instituto Superior Técnico, Technical University of Lisbon, Av. Rovisco Pais, 1, 1049-001 Lisboa, Portugal
e-mail: susana.ramalho@ist.utl.pt; almoura@math.ist.utl.pt; agambar@math.ist.utl.pt; adelia.sequeira@math.ist.utl.pt

U. Ledzewicz et al., *Mathematical Methods and Models in Biomedicine*, Lecture Notes on Mathematical Modelling in the Life Sciences, DOI 10.1007/978-1-4614-4178-6_6,

Blood is a concentrated suspension of formed cellular elements that includes red blood cells (RBC or erythrocytes), white blood cells (or leukocytes), and platelets (or thrombocytes), suspended in an aqueous polymer solution, the plasma. RBC have been shown to exert the most significant influence on the mechanical properties of blood, mainly due to their high concentration (hematocrit $H_t \approx$ 40–45%). Consequently, the rheology of blood is largely affected by the behavior of the RBC, which can range from 3D microstructures to dispersed individual cells, depending predominantly on the shear rates [24]. Hemodynamics is not only related to the fluid properties but also to other mechanical factors, including the forces exerted on the fluid, the fluid motion, and the vessel geometry.

According to the circulatory region of interest and the desired level of accuracy, blood flow may be modeled as steady or pulsatile, Newtonian or non-Newtonian, and laminar or turbulent. In medium to large vessels, blood flow has pulsatile behavior, due to the repeated, rhythmic mechanical pumping of the heart [15]. However, in small arteries sufficiently distant from the heart the flow is predominantly steady. In this work, the importance of including the pulsatility of blood is studied, and both steady and unsteady simulations are considered.

As mentioned above, the RBC play an important role in the blood rheology. While plasma exhibits a nearly Newtonian behavior, whole blood has non-Newtonian characteristics [22]. This is mainly due to the RBC's tendency to form 3D microstructures at low shear rates and to their deformability and alignment with the flow field at high shear rates. Experimental studies suggest that in most part of the arterial system the viscosity of blood can be considered as a constant, and blood can be modeled as a Newtonian fluid. However, the complex processes related to the formation and breakup of the 3D microstructures, as well as the elongation and recovery of individual RBC, contribute in particular to blood shear-thinning viscosity, corresponding to a decrease in the apparent viscosity with increasing shear rate. It has also been observed that blood can present viscoelastic behavior [1, 22]. The variability of the blood viscosity leads to differences in perceived shear stress along the arterial wall. Indeed, in large arteries the instantaneous shear rate over a cardiac cycle has drastic variations, up to two orders of magnitude [25]. Despite these findings, as referred, it is often reasonable to simulate blood flow as a Newtonian fluid, since in sufficiently large nonpathological arteries it experiences high shear rates, over $100\,\mathrm{s}^{-1}$. Many authors adopt this argument however this assumption is not valid when the shear rate is lower than $100\,\mathrm{s}^{-1}$, which is the case of small arteries, veins, capillaries, and aneurysms or in recirculation regions downstream of a stenosis [27]. In these cases the flow is slower and the non-Newtonian models are better suited. Nevertheless, hemodynamics in intracranial aneurysms has been argued to be accurately modeled using the Newtonian assumption [4]. Here, both Newtonian and non-Newtonian fluid mathematical models will be adopted and compared.

Variations in the mathematical modeling of blood rheology lead to modeling uncertainties, which might compromise the reproducibility of the clinical data. The present work also focuses on the uncertainties that arise from considering different boundary conditions at the outflow sections of the computational domain, as well as from the inclusion or exclusion of the main side-branches in the geometry. The geometries employed in this work consist of a patient-specific aneurysm, obtained from medical imaging, and an idealization, for comparison purposes.

The outline of this chapter is as follows. Section 2 is dedicated to the geometry reconstruction of the patient-specific medical image data. The idealization of the anatomically realistic geometry will be also discussed. Section 3 is devoted to the detailed description of the mathematical models. It includes the description of the three-dimensional (3D) fluid model, as well as the reduced one-dimensional (1D), and zero-dimensional (0D) models. The couplings of the reduced models with the 3D one, that serve here as proper outflow boundary conditions, are also discussed. The numerical methods, geometry specifications, and inflow boundary conditions are introduced in Sect. 4. In Sect. 5 the numerical results are presented and discussed. Finally, in Sect. 6 conclusions are drawn.

2 Geometries Definition

The numerical simulations of hemodynamics are performed on both idealized geometries and an anatomically realistic geometry of a patient-specific aneurysm. The patient-specific geometry is reconstructed from medical images obtained in vivo from rotational computerized tomography angiography (CTA), with resulting voxel resolution of 0.4 mm on a 512^3 grid. This volumetric data is segmented using a constant threshold value. The surface triangulation of the vessel wall is extracted using a marching tetrahedra algorithm and hence a linear interpolation. This approach is computationally inexpensive but assumes that the image intensity of the desired object is sufficiently different from the background to permit a constant gray scale threshold choice. It furthermore requires that the medical image resolution is fine enough and isotropic to perform marching tetrahedra directly, instead of performing an interpolation as presented in [8] and references therein.

Several other segmentation methods exist for image data of cerebral aneurysms, such as deformable models and region growing [2, 4, 23]; however these tend to be sensitive to user defined parameter settings. Each segmentation approach will yield a different geometry definition that depends on user-defined coefficients or assumptions made in the approach [26]. Ultimately there is an inherent uncertainty in the model definition limited by the acquisition modality, resolution, contrast, and noise.

The resulting virtual model of the vasculature is then prepared for the numerical simulations by identifying the regions of interest and removing secondary branches. Successively surface smoothing is performed due to medical imaging noise and limited resolution, taking care not to alter the object beyond the pixel size, since this represents the inherent uncertainty size. Smoothing is performed using the bi-Laplacian method, with a final inflation along the local normal by a constant distance in order to minimize the volume alteration and surface distortion [8].

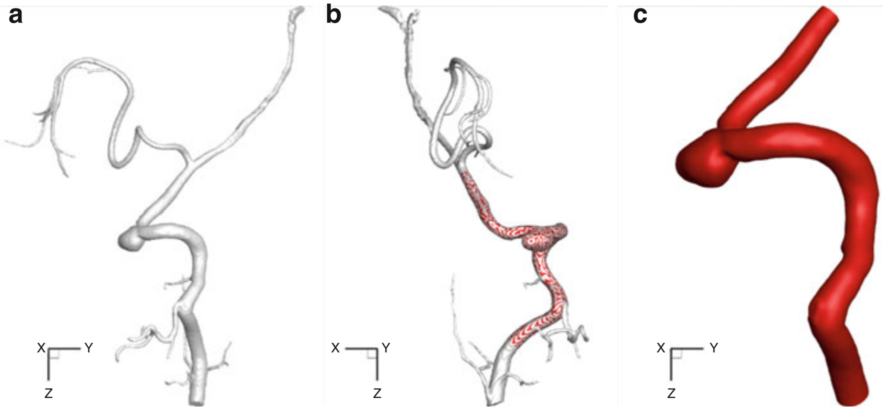

Fig. 1 Cerebral arterial system showing a saccular aneurysm located on the outer bend of the posterior inferior cerebral artery (PICA) in (**a**) coronal view, (**b**) sagittal view with superposition of the region of interest,and (**c**) detail of the region of interest in coronal view

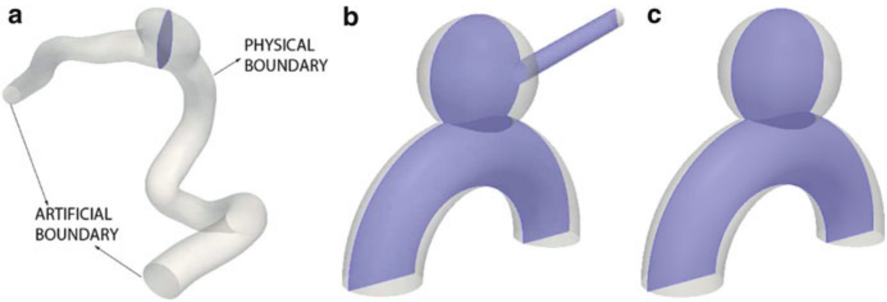

Fig. 2 The geometries considered, including the chosen cross-sections: (**a**) region of interest of the anatomically realistic geometry with side-branches excluded; (**b**) idealized geometry with side-branch in the aneurysm; (**c**) idealized geometry with hole (clipped side-branch) in the aneurysm

The anatomically realistic geometry of the aneurysm and the identification of the region of interest for the computational domain are depicted in Fig. 1. The idealized geometry considered is inspired from [11]. It has a reduced surface definition complexity, introducing however a side-branch in the aneurysm. The aim is to provide a clearer understanding of the sensitivity to the choice of fluid boundary conditions in a similar flow field to that of the anatomically realistic geometry. Nonetheless, the idealization reduces the presence of complex flow structures that arise in the patient-specific case, due to the non-planarity of the main vessel and the small-scale detail in the surface definition. The idealized geometry consists of a main vessel with constant diameter and radius of curvature, a spherical saccular aneurysm, and a side-branch that is represented by either a straight tube or a hole, resulting in a total of two idealized geometries. Figure 2 shows the geometries studied: anatomically realistic, idealized with tube side-branch, and idealized with hole side-branch. For abbreviation these geometries will be referred to as "real," "idealized with branch," and "idealized with hole," respectively.

3 The Mathematical Models

Hemodynamics in the cardiovascular system is modeled through the time-dependent equations for incompressible fluids, derived from the conservation of momentum and mass. They describe a homogeneous fluid in terms of the velocity and the pressure fields. Considering an open and bounded domain $\Omega \subset \mathbb{R}^3$, the system of equations representing such fluid is given by

$$\begin{cases} \dfrac{\partial \mathbf{u}}{\partial t} + (\mathbf{u} \cdot \nabla)\,\mathbf{u} - \dfrac{1}{\rho}\mathbf{div}\,\boldsymbol{\sigma}(p,\mathbf{u}) = \mathbf{f}, & \\ & \text{in} \quad \Omega, \forall t > 0, \\ \operatorname{div}\mathbf{u} = 0, & \end{cases} \tag{1}$$

where $\mathbf{f}$ represents the body forces (that will be neglected, $\mathbf{f} = \mathbf{0}$, for the case study at hand), ρ is the fluid constant density, and the Cauchy stress tensor $\boldsymbol{\sigma}(p,\mathbf{u})$ depends on the unknown fluid pressure, p, and velocity, $\mathbf{u}$, and may be generally represented as the sum of the so-called spherical, $p\mathbf{I}$, and deviatoric, $\boldsymbol{\tau}(\mathbf{D}(\mathbf{u}))$, parts [21]

$$\boldsymbol{\sigma}(p,\mathbf{u}) = -p\mathbf{I} + \boldsymbol{\tau}(\mathbf{D}(\mathbf{u})). \tag{2}$$

In the spherical part, p is the Lagrange multiplier associated to the incompressibility constraint $\mathbf{div}(\mathbf{u})$, which defines the mechanical pressure for incompressible fluids, $p = p(\mathbf{x},t)$, and $\mathbf{I}$ is the unitary tensor. Concerning the deviatoric tensor, $\boldsymbol{\tau}$, it depends on the strain rate tensor, $\mathbf{D}(\mathbf{u})$, which is the symmetric part of the velocity gradient

$$\mathbf{D}(\mathbf{u}) = \frac{1}{2}\left(\nabla\mathbf{u} + (\nabla\mathbf{u})^{\mathrm{T}}\right).$$

3.1 Newtonian Fluids

The definition of a constitutive relation for $\boldsymbol{\tau}(\mathbf{D}(\mathbf{u}))$ is related to the rheological properties of the fluid. Under the assumption of incompressible Newtonian fluids, the Cauchy stress tensor is a linear isotropic function of the components of the velocity gradient, and it is given by

$$\boldsymbol{\sigma}(\mathbf{u},p) = -p\mathbf{I} + 2\mu\mathbf{D}(\mathbf{u}), \tag{3}$$

where $\mu > 0$ is the fluid constant Newtonian viscosity and $\boldsymbol{\tau}(\mathbf{u}) = 2\mu\mathbf{D}(\mathbf{u})$.

Thus, applying the constitutive relation (3) to Eq. (1), the Navier–Stokes equations for incompressible Newtonian fluids are obtained:

$$\begin{cases} \rho \dfrac{\partial \mathbf{u}}{\partial t} + \rho\,(\mathbf{u}\cdot\nabla)\,\mathbf{u} + \nabla p - \operatorname{div}(2\mu\mathbf{D}(\mathbf{u})) = \mathbf{0}, \\ \qquad\qquad\qquad\qquad\qquad\qquad\qquad\qquad \operatorname{div}\,\mathbf{u} = 0. \end{cases} \quad \text{in} \quad \Omega, \forall t > 0, \tag{4}$$

3.2 Generalized Newtonian Fluids

The most general form of Eq. (2), for isotropic symmetric tensor functions, under frame invariance requirements [21], is given by

$$\boldsymbol{\sigma} = \phi_0\mathbf{I} + \phi_1\mathbf{D} + \phi_2\mathbf{D}^2, \tag{5}$$

with ϕ_0, ϕ_1, and ϕ_2 dependent on the density ρ and on the three principal invariants of $\mathbf{D}$, $\mathbf{I}_D = tr(\mathbf{D})$, $\mathbf{II}_D = \frac{1}{2}\left((tr(\mathbf{D}))^2 - tr(\mathbf{D}^2)\right)$, and $\mathbf{III}_D = det(\mathbf{D})$, where $tr(\mathbf{D})$ and $det(\mathbf{D})$ denote the trace and the determinant of tensor $\mathbf{D}$, respectively. By setting $\phi_2 = 0$, and ϕ_1 constant, we obtain the relation for a Newtonian fluid, governed by the Navier-Stokes equations (4). Considering $\phi_2 \neq 0$ does not correspond to any existent fluid under simple shear, so that the constitutive relation (5) is often used in the reduced general form, with $\phi_2 = 0$ [21]: $\boldsymbol{\sigma} = \phi_0\mathbf{I} + \phi_1\mathbf{D}$. Moreover, respecting the frame invariance requirements and the behavior of real fluids, ϕ_1 becomes the viscosity function [21], and the following general constitutive relation is obtained:

$$\boldsymbol{\sigma} = -p\mathbf{I} + 2\mu(\mathbf{II}_D, \mathbf{III}_D)\mathbf{D}, \tag{6}$$

where the viscosity function μ might depend on the second and third invariants of $\mathbf{D}$.

Since $\mathbf{III}_D = 0$ in simple shear, as well as in other viscometric flows, it is reasonable to neglect the dependence of μ on $\mathbf{III}_D$. Furthermore, $\mathbf{II}_D$ is negative for isochoric motions, where $tr(\mathbf{D}) = 0$, so the positive metrics of the rate of deformation

$$\dot{\gamma} \equiv \sqrt{-4\mathbf{II}_D} = \sqrt{2tr(\mathbf{D}^2)},$$

also known as the shear rate, may be defined. Using the definition of the shear rate as a function of the second invariant of $\mathbf{D}$, relation (6) can be rewritten as follows:

$$\boldsymbol{\sigma} = -p\mathbf{I} + 2\mu(\dot{\gamma})\mathbf{D}. \tag{7}$$

This equation defines the constitutive equation for the generalized Newtonian fluids, such that the equations of motion for these fluids are of the form

Table 1 Some generalized Newtonian models for blood viscosity and corresponding constants

Model	Viscosity model	Model constants for blood
Carreau	$F(\dot{\gamma}) = (1+(\lambda\dot{\gamma})^2)^{(n-1)/2}$	$\mu_0 = 0.456, \mu_\infty = 0.032$ $\lambda = 10.03\,s, n = 0.344$
Cross	$F(\dot{\gamma}) = (1+(\lambda\dot{\gamma})^m)^{-1}$	$\mu_0 = 0.618, \mu_\infty = 0.034$ $\lambda = 7.683\,s, m = 0.810$
Yeleswarapu	$F(\dot{\gamma}) = \dfrac{1+\log(1+\lambda\dot{\gamma})}{1+\lambda\dot{\gamma}}$	$\mu_0 = 1.10, \mu_\infty = 0.035$ $\lambda = 45.23\,s$
Oldroyd	$\mu(\dot{\gamma}) = \mu_0 \dfrac{1+(\lambda_1\dot{\gamma})^2}{1+(\lambda_2\dot{\gamma})^2}$	$\mu_0 = 0.426, \mu_\infty = \mu_0\lambda_1^2\lambda_2^{-2}$ $\lambda_1 = 1.09\,s, \lambda_2 = 3.349\,s$

$$\begin{cases} \rho \dfrac{\partial \mathbf{u}}{\partial t} + \rho\,(\mathbf{u}\cdot\nabla)\,\mathbf{u} + \nabla p - \mathrm{div}(2\mu(\dot{\gamma})\mathbf{D}(\mathbf{u})) = \mathbf{0}, & \\ & \text{in} \quad \Omega, \forall t > 0, \\ \mathrm{div}\,\mathbf{u} = 0. & \end{cases} \tag{8}$$

A variety of non-Newtonian viscosity functions $\mu(\dot{\gamma})$ can be used, only differing on the functional dependence of the viscosity μ on the shear rate $\dot{\gamma}$. To model blood flow, the focus is put on bounded viscosity functions of the form

$$\mu(\dot{\gamma}) = \mu_\infty + (\mu_0 - \mu_\infty)\mathrm{F}(\dot{\gamma}), \tag{9}$$

where the constants μ_0 and μ_∞ are the asymptotic viscosities at zero, $\mu_0 = \lim_{\dot{\gamma}\to 0}\mu(\dot{\gamma})$, and infinity, $\mu_\infty = \lim_{\dot{\gamma}\to\infty}\mu(\dot{\gamma})$, shear rate. $\mathrm{F}(\dot{\gamma})$ is a continuous and monotonic function such that

$$\lim_{\dot{\gamma}\to 0}\mathrm{F}(\dot{\gamma}) = 0, \qquad \lim_{\dot{\gamma}\to\infty}\mathrm{F}(\dot{\gamma}) = 1. \tag{10}$$

The definition of function $\mathrm{F}(\dot{\gamma})$ characterizes the generalized Newtonian model. Table 1 was taken from [9] and shows several possible viscosity functions.

The values of the parameters there displayed, corresponding to an hematocrit $H_t = 40\,\%$ and temperature $T = 37\,°\mathrm{C}$, were obtained from in vitro blood experimental data, as described in [9]. To set the parameters values, a nonlinear least squares fitting was applied [9, 13]. Notice that, with such parameters, all the viscosity functions in Table 1 correspond to shear-thinning models.

Other generalized Newtonian models for blood viscosity, like the power-law and the Carreau–Yasuda model, have been frequently used to describe blood flow (for further details on these models, see [22]). In this work, following [9, 13], the Carreau viscosity function is used, with the parameters provided in Table 1.

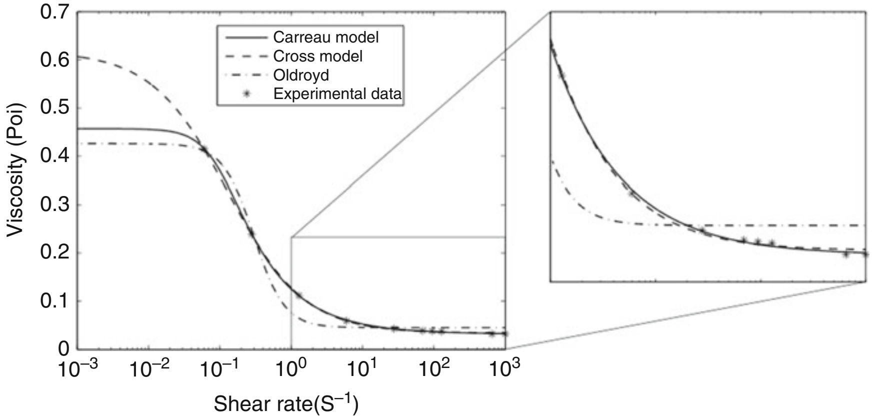

Fig. 3 Apparent viscosity as a function of shear rate for whole blood at $H_t = 40\,\%$, T = 37 °C, taken from [9]

Plots of some non-Newtonian models and the experimental data are shown in Fig. 3. Experimental data for low shear rates is difficult to obtain, resulting in very different behavior as the shear rate approaches zero.

3.3 Outflow Boundary Conditions

Equations (4) or (6) have to be provided with initial and boundary conditions, in order to be mathematically well defined and prepared to be solved by numerical methods. The prescription of proper initial and boundary conditions is a crucial step in the numerical procedure to obtain accurate and meaningful computed solutions.

After defining the initial condition, $\mathbf{u} = \mathbf{u}_0$, for $t = 0$ in Ω, an appropriate set of conditions must be imposed on the boundary of the domain Ω. In particular, for the problem of blood flow in arteries, the computational domain is bounded by a physical boundary that is the arterial wall, and by artificial boundaries on the fluid domain due to truncation of the artery, detailed in Fig. 2.

On the physical boundary corresponding to the vascular wall a no-slip condition is imposed, describing the complete adherence of the fluid to the wall. In this study, the compliance of the artery wall will be neglected, that is, a fixed geometry is considered, so that the velocity at the wall is zero. Thus, an homogeneous Dirichlet boundary condition, $\mathbf{u} = \mathbf{0}$, $\forall t > 0$, is imposed at the physical wall of the fluid.

The boundary conditions at the artificial sections cannot be obtained from physical arguments and can be a significant source of numerical inaccuracies in resolving the problem [3]. At these interfaces the remaining parts of the arterial system need to be accounted for and modeled. Typically, it is very difficult to obtain appropriate patient data for the flow boundary conditions.

In this work a traction free boundary condition $\sigma(\mathbf{u}, p) \cdot \mathbf{n} = 0$ will always be considered at the main vessel outflow (see Fig. 2b). Concerning the outflow section of the side-branch, four types of outflow boundary conditions are explored: zero velocity, $\mathbf{u} = \mathbf{0}$, meaning that the side-branch is neglected and modeled as a no-slip wall [19]; zero normal stress, $\sigma(\mathbf{u}, p) \cdot \mathbf{n} = 0$ [4]; coupling with a 0D model corresponding to a simple resistance [13]; and coupling with a one-dimensional (1D) model equivalent to the three-dimensional (3D) side-branch [6]. Thus, the first two approaches neglect the effects of the remaining parts of the cardiovascular system, as opposed to the last two which resort to the Geometrical Multiscale Approach [6] to account for the global circulation on the localized numerical simulation.

3.4 The 1D Model

The 1D simplified model is formulated assuming that an artery is a cylindrical compliant tube, with axial symmetry and fixed cylinder axis. The velocity components orthogonal to the vessel axis are neglected and the wall displacements are only accounted for in the radial direction. Moreover, no body forces are considered and the pressure, $P(t,z)$, is assumed constant on each axial section, varying only coaxially. The area of each cross-section S is given by $A(t,z) = \int_S d\sigma$, and the mean velocity is defined as $\bar{u} = A^{-1} \int_S u_z d\sigma$, where u_z is the axial velocity. The area, A, the averaged pressure, P, and the mean flux, $Q = A\bar{u}$, are the unknown variables to be determined. The average pressure and flow rate are related to the 3D pressure and velocity, respectively, while the area is related to the 3D wall displacement. Thus, the 1D model provides a fluid–structure interaction (FSI) description of blood flow in arteries, accounting for the wall compliance due to the blood load. For that reason, the 1D model captures very well the wave propagation nature of blood flow in arteries.

Integrating the Navier–Stokes equations on a generic cross-section S of the cylindrical vessel, and after the above mentioned simplifications, explored in [6], the reduced 1D form of the continuity and momentum equations for the flow of blood in arteries is given, for all $t > 0$, by

$$\begin{cases} \dfrac{\partial A}{\partial t} + \dfrac{\partial Q}{\partial z} = 0, \\ \dfrac{\partial Q}{\partial t} + \alpha \dfrac{\partial}{\partial z}\left(\dfrac{Q^2}{A}\right) + \dfrac{A}{\rho}\dfrac{\partial P}{\partial z} + K_r\left(\dfrac{Q}{A}\right) = 0, \end{cases} \quad z \in (a,b), \tag{11}$$

where z is the axial direction, $L = b - a$ denotes the vessel length, K_r is the friction parameter, α is the momentum flux correction coefficient, also known as Coriolis coefficient, defined by $\alpha = \frac{\int_S u_z^2 \mathrm{d}\sigma}{A\bar{u}^2}$, and ρ is the fluid mass density. For a parabolic profile, the friction parameter is defined as $K_r = 8\pi\mu$ [6], which is the value generally used in practice. The Coriolis coefficient is set to $\alpha = 1$, corresponding to a flat profile [6], in order to simplify the analysis. The density ρ and the fluid dynamic viscosity μ are considered constant. Hence, the 1D model does not account for the non-Newtonian behavior of blood.

The previous system of two equations for the three unknown variables A, Q, and P needs to be closed. In order to do that, a structural model for the vessel wall movements, relating pressure and area, must be given. Here, the simplest pressure-area algebraic relation [6, 7] is used

$$P(t,z) - P_{\mathrm{ext}} = \beta \frac{\sqrt{A} - \sqrt{A_0}}{A_0}, \tag{12}$$

where A_0 is the initial area and β is a single parameter that describes the mechanical and physical properties of the vessel wall

$$\beta = \frac{\sqrt{\pi} h E}{1 - \xi^2}, \tag{13}$$

where h the wall thickness, E the vessel wall Young, or elasticity, modulus, and ξ the vessel wall Poisson ratio. β is constant along z only when E, h, or A_0 are constant, since they may be functions of z. In this work, the wall parameters are assumed constant along z, and the external pressure is neglected: $P_{\mathrm{ext}} = 0$.

Numerical Discretization of the 1D Model

The 1D model is numerically discretized in time and space by means of a second-order Taylor-Galerkin scheme [6]. It consists in using the Lax-Wendroff scheme to discretize in time and the finite element method to obtain the space approximation. This discretization can be considered as a finite element counterpart of the Lax-Wendroff scheme, which has a very good dispersion error characteristic and can be easily implemented [6].

A uniform mesh is used, meaning that the elements size is constant and equal to h. Moreover, linear ($P1$) finite elements are considered. The Lax–Wendroff scheme is obtained using a Taylor series of the solution $\mathbf{U} = [Q \;\; A]^{\mathrm{T}}$ truncated to the second order, resulting in an explicit scheme. Being an explicit time advancing method, the Lax–Wendroff scheme requires the verification of a condition bounding the time step [6]

$$\Delta t \leq \frac{\sqrt{3}}{3} \frac{h}{\max(c + |\bar{u}|)}, \tag{14}$$

where h is the size of the spatial mesh and $c = c(A;A_0;\beta) = \sqrt{\frac{\beta}{2\rho A_0}}A^{\frac{1}{4}}$ is the speed of the wave propagation along the vessel. Condition (14) corresponds to a CFL number of $\frac{\sqrt{3}}{3}$.

The final finite element solution for the area and flow rate is obtained by finding, at each time step t^{n+1}, $\mathbf{U}_h^{n+1}(z) = \sum_{i=0}^{N+1} \mathbf{U}_i^{n+1}\psi_i(z) \in V_h(a,b)$, where $V_h(a,b)$ is the space of $P1$ finite elements in 1D for the uniform mesh associated to h spacing, and $\{\psi_i\}_{i=1}^N$ its basis, satisfying the following expression for the interior nodes:

$$(\mathbf{U}_h^{n+1},\psi_j) = (\mathbf{U}_h^n,\psi_j) + \Delta t\left(\mathbf{F}^n - \frac{\Delta t}{2}\mathbf{H}^n\mathbf{B}^n, \frac{\partial \psi_j}{\partial z}\right) - \Delta t\left(\mathbf{B}^n - \frac{\Delta t}{2}\mathbf{B}_{\mathbf{U}}^n\mathbf{B}^n,\psi_j\right)$$
$$-\frac{\Delta t^2}{2}\left(\mathbf{H}^n\frac{\partial \mathbf{F}^n}{\partial z}, \frac{\partial \psi_j}{\partial z}\right) + \frac{\Delta t^2}{2}\left(\mathbf{B}_{\mathbf{U}}^n\frac{\partial \mathbf{F}^n}{\partial z},\psi_j\right),\ j = 1,\cdots,N, n = 0,\cdots,M-1. \tag{15}$$

Here $\mathbf{U}_h^0$ is a suitable approximation of the initial data, $(\mathbf{u},\mathbf{v}) := \int_a^b \mathbf{u}\cdot\mathbf{v}\mathrm{d}z$ represents the inner product in $V_h(a,b)$, $\{\psi_j\}_{j=1}^N$ are the basis functions of $V_h(a,b)$, $\Delta t = t^{n+1} - t^n$, and

$$\mathbf{H} = \begin{bmatrix} 0 & 1 \\ -\alpha\frac{Q^2}{A^2} + \frac{\beta}{2\rho A_0}A^{\frac{1}{2}} & 2\alpha\frac{Q}{A} \end{bmatrix}, \quad \mathbf{B}_{\mathrm{U}} = \begin{bmatrix} 0 & 0 \\ K_r\frac{Q}{A^2} & -K_r\frac{1}{A} \end{bmatrix},$$

$$\mathbf{F} = \begin{bmatrix} Q \\ \alpha\frac{Q^2}{A} + \frac{\beta}{3\rho A_0}A^{\frac{3}{2}} \end{bmatrix}, \qquad \mathbf{B} = \begin{bmatrix} 0 \\ -K_r\frac{Q}{A} \end{bmatrix}.$$

System (15) must be supplemented with proper initial, $\mathbf{U}_h^0$, and boundary conditions for the solution $\mathbf{U}_h^{n+1}$, at the left and right boundary points, $z = a$ and $z = b$, respectively. In the present work, the initial conditions were taken to be $A^0(z) = A_0$ and $Q^0(z) = 0$.

Compatibility Conditions for the 1D Model

By choosing relation (12), the pressure may be eliminated from the momentum equation, and system (11) becomes hyperbolic, with two distinct eigenvalues (see [6, 17] for the characteristic analysis of system (11))

$$\lambda_{1,2} = \bar{u} \pm c, \tag{16}$$

where c is the speed of the propagation of waves along the artery, defined above. The eigenfunctions, or characteristic variables, corresponding to the eigenvalues $\lambda_{1,2}$, are defined by

Fig. 4 The characteristic lines

$$W_{1,2} = \bar{u} \pm \int_{A_0}^{A} \frac{c(\tau)}{\tau} \mathrm{d}\tau = \bar{u} \pm 4\sqrt{\frac{\beta}{2\rho A_0}}\left(A^{\frac{1}{4}} - A_0^{\frac{1}{4}}\right). \tag{17}$$

Under physiological conditions, typical values of the flow velocity and mechanical characteristics of the vessel wall are such that $c \gg \bar{u}$, and consequently we have that $\lambda_1 > 0$ and $\lambda_2 < 0$, everywhere. This means that the flow is subcritical, such that the characteristic variable W_1 associated to the first eigenvalue, λ_1, travels forward, while the characteristic variable W_2, associated to the second eigenvalue, λ_2, travels backward (see Fig. 4). Hence, W_1 is the incoming characteristic, and W_2 is the outgoing characteristic, at the upstream left point ($z = a$), and vice versa at the downstream right point ($z = b$), as illustrated in Fig. 4.

Because of this, exactly one boundary condition must be imposed at each extremity of the vessel [18]. However, the discretized model requires two conditions at each boundary node in order to solve the system, corresponding to Q_h^{n+1} and A_h^{n+1}, both at $z = a$ and $z = b$. Thus two additional conditions, which have to be compatible with the problem, are needed at the numerical level. These compatibility conditions can be obtained by means of the outgoing characteristic at each boundary [18], through projecting the equations along the characteristic lines exiting the domain [16]. This results in computing the following additional relations at the boundaries:

$$W_2(Q_h^{n+1}(a), A_h^{n+1}(a)) = W_2(Q_h^n(z_a), A_h^n(z_a)) - \Delta t K_r \frac{Q_h^n(z_a)}{(A_h^n(z_a))^2}, \quad \text{at } z = a, \tag{18}$$

and

$$W_1(Q_h^{n+1}(b), A_h^{n+1}(b)) = W_1(Q_h^n(z_b), A_h^n(z_b)) - \Delta t K_r \frac{Q_h^n(z_b)}{(A_h^n(z_b))^2}, \quad \text{at } z = b, \tag{19}$$

where z_a and z_b are the corresponding foot of the outgoing characteristic lines which, using a first-order approximation [6], are given by

$$z_a = a - \Delta t \lambda_2(Q_h^n(a), A_h^n(a)) = a - \Delta t\left(\frac{Q_h^n(a)}{A_h^n(a)} + \sqrt{\frac{\beta}{2\rho A_0}}(A_h^n(a))^{\frac{1}{4}}\right), \tag{20}$$

$$z_b = b - \Delta t \lambda_1(Q_h^n(b), A_h^n(b)) = b - \Delta t\left(\frac{Q_h^n(b)}{A_h^n(b)} - \sqrt{\frac{\beta}{2\rho A_0}}(A_h^n(b))^{\frac{1}{4}}\right). \tag{21}$$

The solution for the boundary nodes of the domain may then be achieved through resolving a 2×2 nonlinear system given by Eqs. (18) and (19) (for more details see [17]).

Typically, the inflow condition is a flux or a total pressure, while the outflow condition is given by $W_2 = 0$, such that there is no incoming characteristic at $z = b$, corresponding to a completely absorbing boundary condition at the outflow point.

3D–1D Coupling

To couple the artificial boundary, denoted Γ_{art} from here on, of the 3D fluid Eq. (1) with the 1D interface point $z = a$ of the hyperbolic model (11), the continuity of the flow rate and the mean pressure are imposed, for all $t > 0$ (see for instance [7])

$$\int_{\Gamma_{\text{art}}} \mathbf{u} \cdot \mathbf{n} d\gamma = Q^{1D}(a,t), \tag{22}$$

$$\frac{1}{|\,\Gamma_{\text{art}}\,|} \int_{\Gamma_{\text{art}}} p d\gamma = P^{1D}(a,t). \tag{23}$$

Here $\mathbf{u}$ and p denote the 3D velocity vector and pressure, respectively, and Q^{1D} and P^{1D} are the 1D flow rate and mean pressure, respectively. The solution of the coupled problem is approximated in an iterative way, by resorting to a splitting strategy. This means that each model is solved separately and yields the resultant information to the other. Thus, at each time step the 3D model returns pointwise data, which is integrated to obtain the averaged quantities to be provided to the 1D model as a boundary condition at $z = a$. On the other hand, the 1D model provides the boundary conditions at the coupling sections of the 3D in terms of average data. The average data is defective for the 3D problem, since it requires pointwise data at the coupling interface. Thus, appropriate techniques must be used in order to prescribe the 1D integrated data onto the 3D model as boundary condition. Precisely, in this work the coupling is performed by passing the flow rate from the 3D to the 1D model, imposing Eq. (22) at the coupling point of the 1D model, $z = a$, and by imposing the mean pressure, computed by the 1D model, to the 3D problem, by means of the condition (23) at the 3D artificial coupling boundary, Γ_{art}. To prescribe the defective mean pressure on the 3D coupling section, Γ_{art}, the approach introduced in [12] is followed, so that the mean pressure is imposed through a Neumann boundary condition

$$\sigma(\mathbf{u}, p) \cdot \mathbf{n} = P_{1D}\mathbf{n}, \quad \text{on } \Gamma_{\text{art}}, \quad \forall t > 0. \tag{24}$$

The 3D–1D iterative coupling algorithm is carried out explicitly in this work. At each time step t^n, the 3D model provides the flow rate computed at the previous time step to the 1D model and receives the mean pressure computed from the 1D model. This is followed by advancing to the next time step (see Fig. 5).

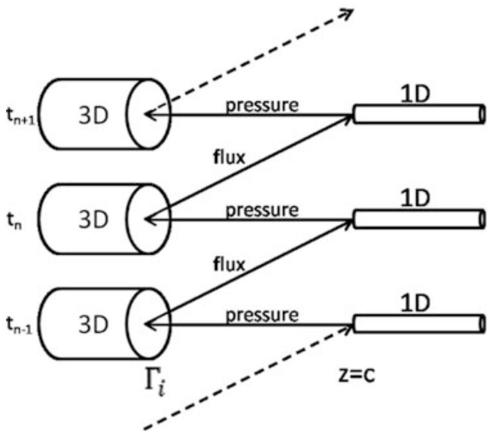

Fig. 5 Scheme of the 3D–1D explicit coupling

3.5 The 0D Model

Lumped parameters models are derived from the 1D ones by further averaging spatially in the coaxial direction [6], thus losing dependence from the spatial coordinates. Because of this, they are also called 0D models. They are represented by a system of ordinary differential equations (ODEs) in time and are analogous to electric circuits, where the flow rate can be identified with the current, the mean pressure with the voltage, and the 3D physical parameters, such as blood viscosity, blood inertia and wall compliance, with the lumped parameters resistance, inductance, and capacitance, respectively [6]. The 0D models are able to represent the circulation in large compartments of the cardiovascular system, such as the venous bed, the pulmonary circulation, or the heart [6].

In the present study a simple 0D model is also used and coupled to the 3D model. It consists of a single resistance, resulting in an algebraic relation between flux and mean pressure, through the resistance parameter: $P = RQ$. This model is constructed using the linear counterpart of the absorbing boundary condition for the 1D model [13]. Precisely, given the expression (17) of W_2, the condition $W_2 = 0$ is equivalent to

$$f(P) = \sqrt{\frac{8\beta}{\rho A_0}} \left(P\frac{A_0}{\beta} + \sqrt{A_0} \right)^2 \left(\sqrt{P\frac{A_0}{\beta} + \sqrt{A_0}} - A_0^{\frac{1}{4}} \right) = Q. \tag{25}$$

A linearization of expression (25) is obtained resorting to the first approximation around zero of $f(P) : Q = f(P) = f(0) + f'(0)P$ (see [13]). The pressure is then given by

$$P = \frac{\sqrt{\rho\beta}}{\sqrt{2}A_0^{5/4}} Q. \tag{26}$$

3D–0D Coupling

The coupling of the 0D model (26) with the 3D fluid equations corresponds to imposing the linear counterpart of the absorbing boundary condition for the 1D model, $W_2 = 0$, directly on the 3D artificial section. The coupling is achieved by forcing the pressure given by the resistance of the 0D model at the 3D interface section Γ_{art}, similarly to the 3D–1D coupling. An explicit coupling is applied, meaning that the mean pressure at the current time step, P^{n+1}, is computed by means of expression (26) using the flow rate on the artificial section at the previous time step, Q^n, and it is prescribed at the artificial section at the current time step. Thus, as in [13], the defective averaged data condition

$$P^{(n+1)} = \frac{\sqrt{\rho\beta}}{\sqrt{2}A_0^{5/4}} Q^{(n)}, \quad \text{on } \Gamma_{\text{art}}, \tag{27}$$

is prescribed by means of a Neumann boundary condition (24) on the 3D artificial section.

4 Numerical Simulation Setup

In this work, the hemodynamics inside an intracranial saccular aneurysm is analyzed in an anatomically realistic geometry, as well as in idealized geometries. The idealized geometries serve as test cases with reduced complexity of the flow field, allowing for a better understanding of the effects of changing the fluid models, the boundary conditions, and in evaluating steady and unsteady simulations. Moreover, the numerical simulations in the idealized geometries have lower computational costs than in the realistic ones, allowing to conduct a comprehensive series of tests. While clinical decisions should be based on numerical simulations using anatomically realistic patient-specific geometries, idealized models provide insight into the hemodynamics with respect to choices in modeling and numerical setup.

In both steady and unsteady cases, the fluid is initially at rest and then the inflow flow rate is linearly increased with a parabolic profile to a final steady-state flux $Q = 2.67\,\text{cm}^3\,\text{s}^{-1}$, such that

$$Q_{\text{in}}^{\text{ramp}}(t) = \frac{t\,Q}{t_{\text{ramp}}}, \quad \text{for } t < t_{\text{ramp}}, \tag{28}$$

$$Q_{\text{in}} = Q, \quad \text{for } t > t_{\text{ramp}}, \tag{29}$$

where t_{ramp} is the time length of the linear ramp, and it is set to $t_{\text{ramp}} = 1\,\text{s}$ in all test cases. The reference value for the inflow condition, $Q = 2.67\,\text{cm}^3\,\text{s}^{-1}$, is obtained through the relationship between flow rate and vessel areas, derived from measurements in internal carotid and vertebral arteries [5].

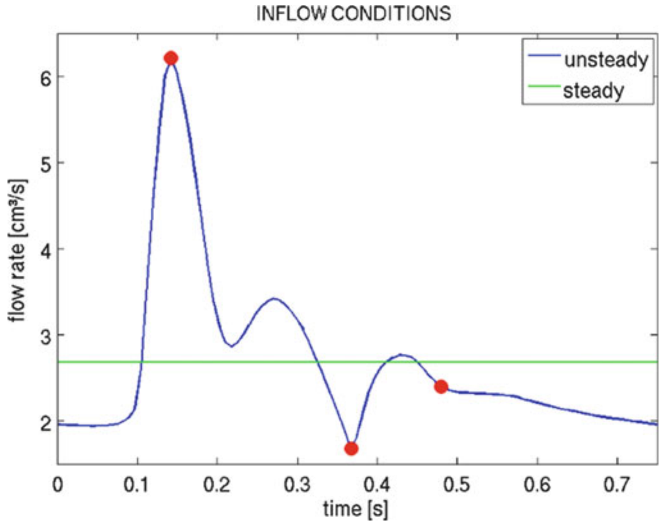

Fig. 6 Steady and unsteady inflow flux profiles versus time. The *points* indicate locations of "peak systole," "minimum diastole" and "mean diastole" used in the discussion section

In the case of pulsatile flow simulations for the idealized geometry, a periodic wave inflow boundary condition is imposed, representing a realistic heart beat waveform, in the carotid, with a mean flux equal to the steady-state flux value. The steady and unsteady inflow flux profiles with respect to time are illustrated in Fig. 6.

Convergent steady-state and pulsatile solutions were identified by checking that the difference between two consecutive time steps (steady case) or two consecutive cycles (unsteady case) was negligible. In the case of the steady state solutions this convergence is of the order of 10^{-7}, while for the unsteady case all the results presented correspond to the 12th cycle where the convergence is of the order of 10^{-6}.

The steady-state simulations were carried out using a time step of 0.01 s, while the pulsatile used a time step of 0.0075 s, corresponding to a hundredth of the heart beating period. Moreover, a time step of 0.5×10^{-4} s was taken when the coupling with the 1D hyperbolic model is used as outflow boundary condition. For both 1D and 0D models, the β parameters used were determined through expression $\beta = \frac{\sqrt{\pi} h_0 E}{1-\xi^2}$, where the thickness of the wall h_0 was set to 10 % of the vessel radius, the Young modulus was set to $E = 10^5$, and the Poisson ratio was set to $\xi = 0.5$, assuming the artery wall is incompressible.

A volumetric mesh of about 0.85 M tetrahedra was created for the anatomically realistic geometry, corresponding to a graded mesh with element size of 0.016 cm within the aneurysm, and maximum size of 0.04 cm in the upstream and downstream sections. The idealized geometries are planar with the parent vessel radius of

0.25 cm, the side-branch radius of 0.075 cm, and the aneurysm radius of 0.4 cm. The side-branch length is 1.2 cm. The idealized geometry volumetric mesh is composed of approximately 0.5 *M* tetrahedral elements, with elements of size 0.02 cm.

5 Discussion

5.1 Idealized Geometry

Hemodynamics inside the idealized aneurysm was studied using the Newtonian and Carreau fluid models, both in steady and unsteady inflow regimes, including and excluding a side-branch within the aneurysm, and prescribing four different types of outflow boundary conditions on the side-branch: traction-free (TF), no-slip (NS), 3D–1D coupling (1D), and 3D–0D coupling (0D). At the outflow section of the main vessel a traction-free boundary condition was always prescribed.

The differences between the Newtonian and Carreau solutions, for both steady and unsteady regimes, are depicted in Fig. 7 (velocity) and Fig. 8 (WSS). The geometry considered for these results is the idealized with hole (clipped side-branch), and the traction-free condition at this outflow boundary. The maximum

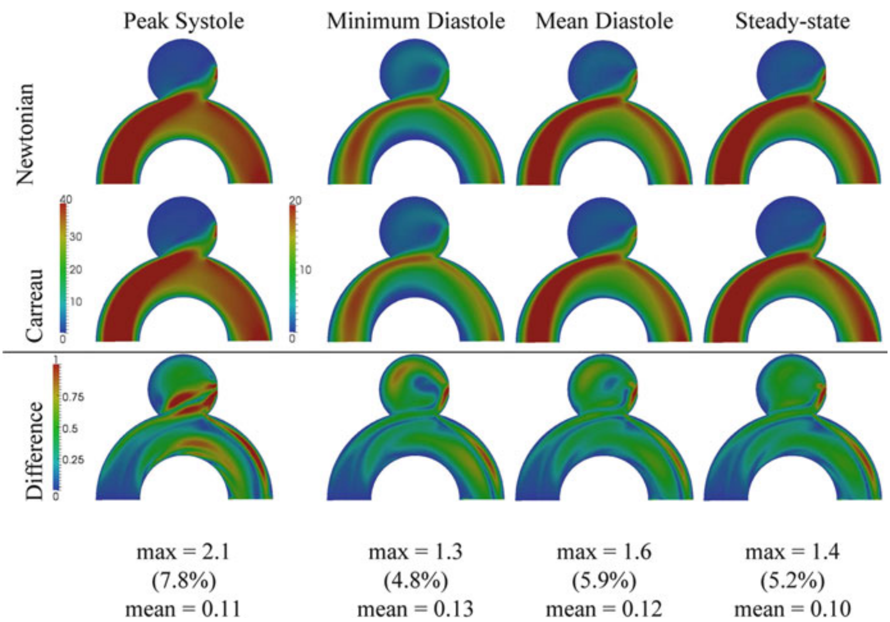

Fig. 7 Velocity magnitude (cm/s) for the clipped geometry with traction-free conditions at the side-branch outflow, using the Newtonian (*top*) and the Carreau (*middle*) models, and its differences (*bottom*), for the unsteady and steady solutions. The maximum difference is calculated for the cross-section, using the maximum value for the percentage

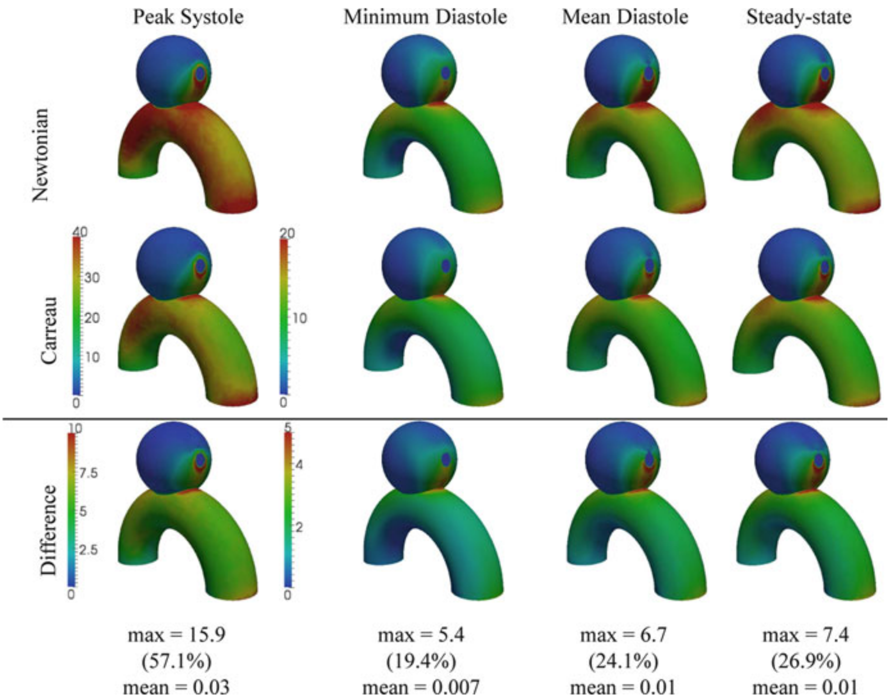

Fig. 8 WSS magnitude (dyn/cm^2) for the clipped geometry with traction-free conditions at the side-branch, using the Newtonian (*top*) and the Carreau (*middle*) models, and its differences (*bottom*), for the unsteady and steady solutions. The maximum difference is calculated for the whole geometry, using the maximum value for the percentage

differences in the velocity cross-section between both models are of the order of 5–8 % and occur inside the aneurysm. The smallest differences occur on the steady case or at the minimum of diastole, while the higher discrepancies are observed during the systolic phase of the unsteady flow. The results show that, even though the average of the difference is low, in some periods of the cardiac cycle the discrepancies between the Newtonian and non-Newtonian models become more noticeable. Comparing the two inflow conditions, the variations that appear inside the aneurysm are higher in all the chosen time instants of the unsteady flow, highlighting the importance of considering simulations as time dependent. The same conclusions can be drawn from the WSS distribution, yet here the discrepancies are more relevant in the main vessel.

In order to analyze the effects of the different outflow conditions, the configuration with the side-branch and a traction-free boundary condition at its outflow is compared with the clipped geometry using all the considered boundary conditions, see Fig. 9 and Table 2. In this particular geometry the side-branch has a substantial influence on the solution, not only due to its location, inside the aneurysm, but also due to the large percentage of flow that enters the branch. The traction-free condition

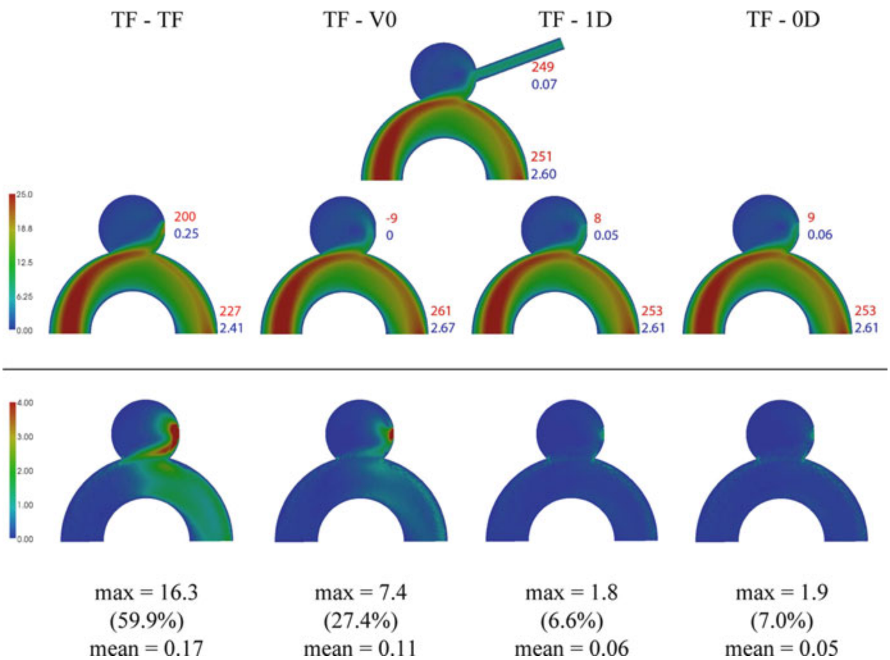

Fig. 9 Velocity magnitude (cm/s) for stead-state simulations of the geometry with side-branch and traction-free boundary condition and the clipped geometry with different boundary conditions and its differences. The maximum difference is calculated on the cross-section, using the maximum value for the percentage. The values in the figure are the pressure drop with the inflow (*red*) and flow rate (*blue*)

Table 2 WSS magnitude differences (dyn/cm^2) for the geometry with side-branch and traction-free boundary condition and the clipped geometry with different boundary conditions

TF - TF	TF - V0	TF - 0D	TF - 1D
Max = 23.5	Max = 13.6	Max = 15.0	Max = 15.0
(81%)	(46.8%)	(51,7%)	(51.7%)
Mean = 4.3e−4	Mean = 8.2e−4	Mean = 4.4e−4	Mean = 4.8e−4

The maximum difference is calculated on the whole geometry, using the maximum value for the percentage

was chosen to be imposed at the end of the side-branch for comparison purposes, here considering the fluid to be fully developed at the branch outflow. From the velocity results of Fig. 9 it is possible to infer that the two reduced models are good approximations of the side-branch, since the differences between imposing these reduced models directly in the clipped configuration and accounting for the side-branch are very small. The disparity between the pressure drops obtained using the reduced 1D and 0D models and the side-branch, are related to the pressure drop across the side-branch. In fact, the pressure drop across the side-branch is 258 dyn/cm^2, which is approximately that found for the reduced models.

These pressure drops, together with the values of the flow rate at the side-branch outflow, indicate that the reduced models provide appropriate outflow boundary conditions, accounting for the side-branch. Prescribing a traction-free condition on the hole section, or neglecting its existence by a $\mathbf{u} = \mathbf{0}$ condition, results in significant discrepancies by considering the branched geometry. Thus, these outflow conditions seem to be worse assumptions than coupling with the reduced models. The differences are more pronounced in the WSS map than in the velocity cross-section, but the minimum difference values are still found when coupling with the reduced models. It is important to notice that despite these larger values, they are confined to the aneurysm at the location of the side-branch, and the average differences are extremely low.

The sensitivity of the computed solution to the boundary condition imposed at the side-branch outflow section is depicted in Figs. 10 and 11, where different outflow conditions are imposed in the clipped geometry. The values of the differences are high, both in the velocity magnitude and in the WSS, except when using the 1D and 0D boundary conditions. From these results it is possible to infer that in this case the calculated resistance of the 0D model is consistent with the 1D model.

As before, the WSS differences are mainly localized close to the side-branch base. In this region the values are very high, yet when considering the average in the whole geometry, the values of the differences decrease abruptly. Thus, as expected, the influence of the side-branch and its outflow boundary condition is particularly important when the side-branch is located very close or within the aneurysm.

Figure 12 displays the differences that exist between the steady-state solution and the time average of the unsteady solution, both for the velocity cross-section and the WSS distribution, in the case of the hole geometry coupled with the 1D model. It is possible to observe that the differences are very small, especially when considering the average. At first sight this could indicate a great resemblance between the steady and unsteady solutions. However, comparing the unsteady solutions of the clipped geometry coupled with the 1D model and the branched geometry with traction-free boundary condition, the differences are magnified at several instants of the cardiac cycle (see Fig. 13). The comparison of these two cases reveals minimal differences for the steady-state inflow conditions, as shown in Fig. 9. Nevertheless, these differences are again significantly higher at different instants of the cardiac cycle, as plotted in Fig. 13. Exhaustive conclusions cannot be drawn from steady-state solutions, since even the average difference of the unsteady solutions of the clipped geometry with the 1D boundary condition and the branched geometry with the traction-free boundary condition is greater than the one for the steady-state. This demonstrates, once again, the relevance of considering unsteady simulations, especially when studying the influence of boundary conditions on the numerical solutions.

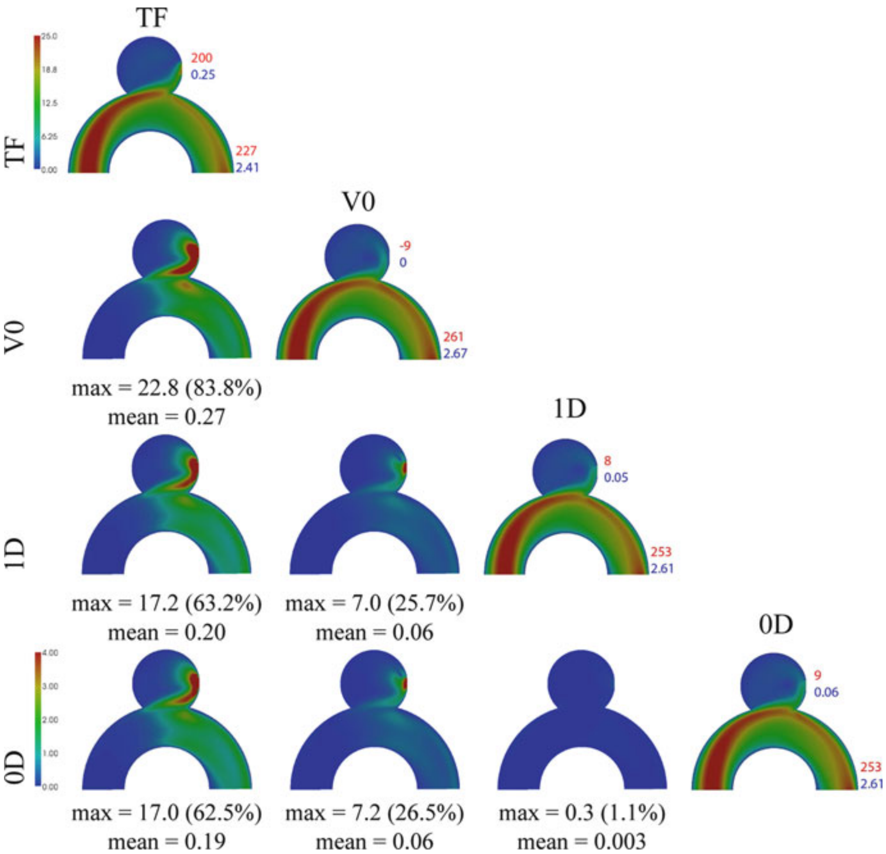

Fig. 10 Velocity magnitude (cm/s) for steady-state simulations of the clipped geometry using different boundary conditions and its differences. The maximum difference is calculated for the cross-section, using the maximum value for the percentage. The values in the figure are the pressure gradient (up) and flow rate (down)

5.2 *Anatomically Realistic Geometry*

The anatomically realistic patient-specific geometry of a cerebral aneurysm (Figs. 1 and 2) was used to study the impact of changing the fluid rheological model. The simulations in this case were performed under a steady inflow regime. As expected also from the results in the idealized geometry, variations in the fluid model influence the computational solution. In Fig. 14 the results for the velocity magnitude, the WSS and WSSG (spatial WSS gradient) for both Newtonian and Carreau solutions are shown, as well as their differences. The discrepancies between the two models reach 11 % in the velocity magnitude inside the aneurysm. The WSS and WSSG differences are even more significant, 19 % and 25 %, respectively, located at the neck of the aneurysm. These results indicate that the use of a constant

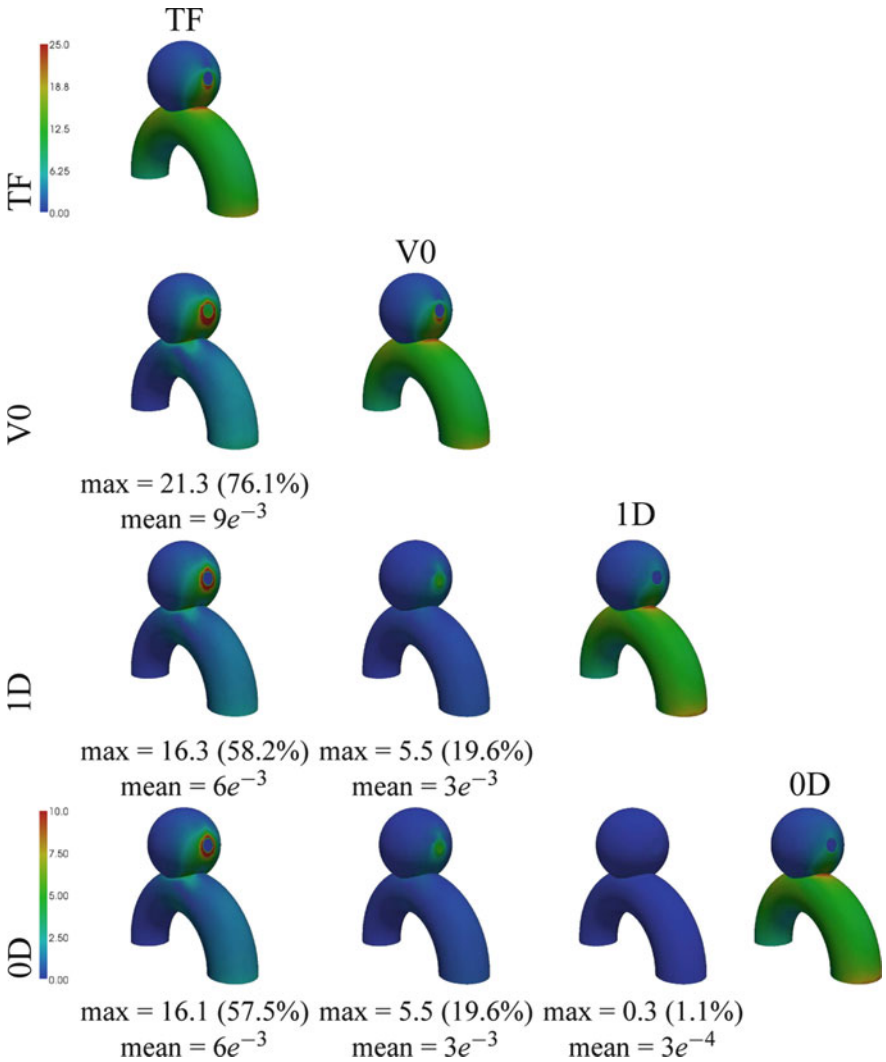

Fig. 11 WSS magnitude (dyn/cm^2) for steady-state simulations of the clipped geometry using different boundary conditions and its differences. The maximum difference is calculated for the whole geometry, using the maximum value for the percentage

viscosity results in overestimated values for the hemodynamic indicators under analysis. Given the special physiological relevance and correlation of low WSS to disease in arteries, the choice of a non-Newtonian model could yield different clinical evaluations. The particle tracing depicted in Fig. 15, where the seeding locations were maintained, shows that the flow structures inside the aneurysm are similar for the Newtonian and non-Newtonian cases; however different locations of

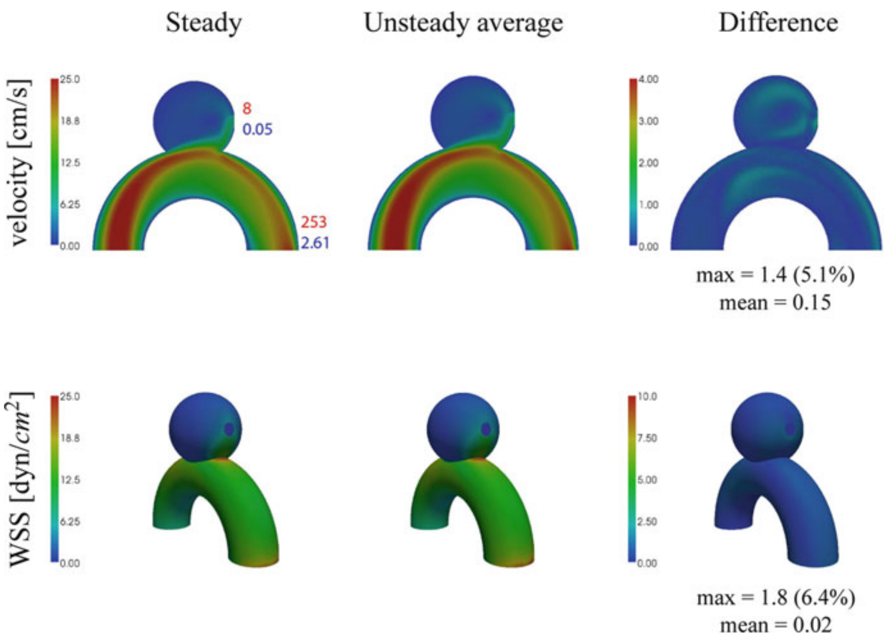

Fig. 12 Velocity (cm/s) and WSS (dyn/cm^2) magnitude for the clipped geometry coupled with the 1D model with time averaged unsteady and steady flow regimes, and corresponding differences

jet impingement and size of the swirling motion are apparent. This indicates that the differences due to the rheological model choice do not only affect the near-wall region, but in cases of complex recirculating flow the free-stream field may also be effectively altered.

6 Conclusions

Two types of geometries were considered: idealized configurations of a curved vessel with an aneurysm, where a side-branch in the aneurysm was included as a tube or a hole, and an anatomically realistic geometry of a cerebral aneurysm with side-branches removed.

Regarding the idealized geometries, both steady and unsteady inflow regimes were considered. Several boundary conditions were prescribed at the outflow section of the side-branch in the aneurysm. Results indicate a large influence of the outflow conditions on the entire domain, but more pronounced near the side-branch base. The reduced 1D and 0D models seem to be fair approaches to take into account the presence of the side-branches, providing appropriate pressure drops. The importance of considering the side-branch increases when located close or in the aneurysm, as it was the case of the idealized geometry.

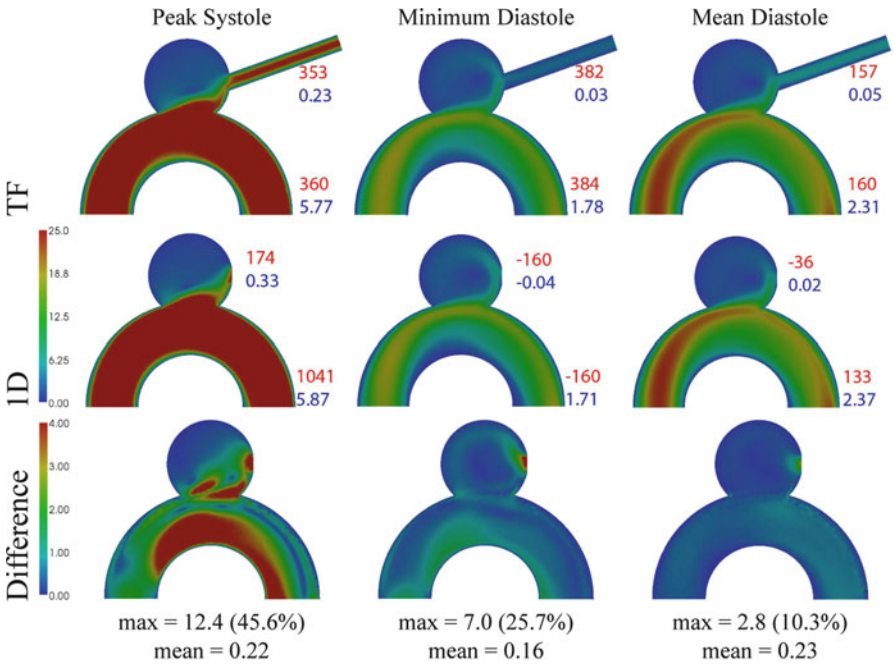

Fig. 13 Velocity magnitude (cm/s) for the geometry with side-branch and traction-free boundary condition and the clipped geometry coupled with the 1D model and its differences, in unsteady flow regime

These conclusions might not be straightforwardly extended to the anatomically realistic geometries, since in such cases the side-branches are not straight tubes. Work is ongoing in applying the approaches here presented to a significant number of patient-specific geometries. The traction-free outflow condition on the clipped geometry compared poorly to the solution of the tube side-branch with a fully developed flow. The differences between steady and unsteady inflow conditions are small and localized when the time averaged solution is compared. However, at specific time instants of the cardiac cycle those differences are much more significant, specially during systole. The Newtonian and Carreau shear-thinning fluid models were used in both realistic and idealized geometries. In both cases differences between the two rheological models are apparent, but less emphatic than the influence of the boundary conditions. Also, the results of the WSS and the WSSG show higher discrepancies between the two blood flow models. The results here presented are preliminary in the sense that they should be complemented with extensive studies in patient-specific geometries in order to obtain conclusions in more general scenarios.

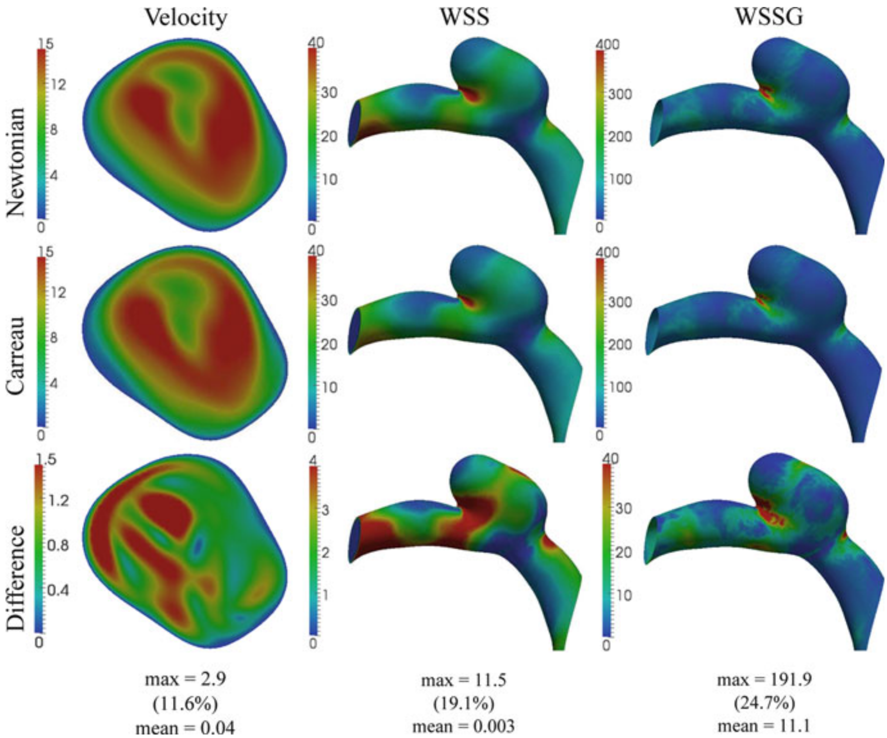

Fig. 14 Results in the realistic geometry for the Newtonian (*top*) and Carreau (*middle*) solutions and their differences (*bottom*). Velocity magnitude (cm/s) in the cross-section depicted in Fig. 2 (*left*), WSS (dyn/cm^2) (*middle*), and WSSG (dyn/cm^2) (*right*). The differences are given in the cross-section for the velocity and over the entire surface for WSS and WSSG. The percentage is calculated using values of the inflow section

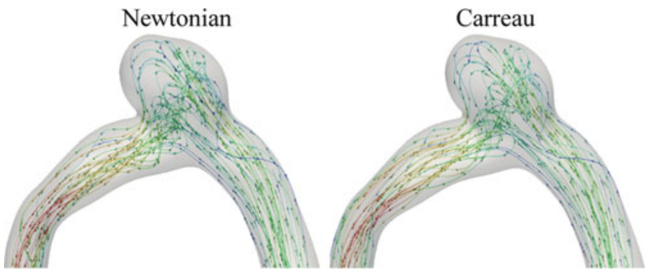

Fig. 15 Particle trace of the Newtonian (*left*) and Carreau (*right*) solutions. Particles are selected at the same location

Acknowledgments We greatly acknowledge Prof. Jorge Campos and his team from the Faculty of Medicine of the University of Lisbon, for providing us the in vivo rotational CTA scans of a specific patient. This work has been partially funded by FCT (Fundação para a Ciência e a Tecnologia, Portugal) through grants SFRH/BPD/34273/2006 and SFRH/BPD/44478/2008 and through the project UT Austin/CA/0047/2008.

References

1. Anand, M., Rajagopal, K.R.: A shear-thinning viscoelastic fluid model for describing the flow of blood. Int. J. Cardiovasc. Med. Sci. **4**(2), 59–68 (2004)
2. Antiga, L., Piccinelli, M., Botti, L., Ene-Iordache, B., Remuzzi, A., Steinman, D.A.: An image-based modeling framework for patient-specific computational hemodynamics. Med. Biol. Eng. Comput. **46**(11), 1097–1112 (2008)
3. Balossino, R., Pennati, G., Migliavacca, F., Formaggia, L., Veneziani, A., Tuveri, M., Dubini, G.: Influence of boundary conditions on fluid dynamics in models of the cardiovascular system: A multiscale approach applied to the carotid bifurcation. Comput. Meth. Biomech. Biomed. Eng. **12**(1) (2009)
4. Cebral, J.R., Castro, M.A., Appanaboyina, S., Putman, C.M., Millan, D., Frangi, A.F.: Efficient pipeline for image-based patient-specific analysis of cerebral aneurysm hemodynamics: Technique and sensitivity. IEEE Trans.Med. Imag. **24**(4), 457–467 (2005)
5. Cebral, J.R., Castro, M.A., Putman, C.M., Alperin, N.: Flow–area relationship in internal carotid and vertebral arteries. Physiol. Meas. **29**, 585 (2008)
6. Formaggia, L., Veneziani, A.: Reduced and multiscale models for the human cardiovascular system. Lecture Notes VKI Lecture Series **7** (2003)
7. Formaggia, L., Moura, A., Nobile, F.: On the stability of the coupling of 3D and 1D fluid-structure interaction models for blood flow simulations. Math. Model. Numer. Anal. **41**(4), 743–769 (2007)
8. Gambaruto, A.M., Peiró, J., Doorly, D.J., Radaelli, A.G.: Reconstruction of shape and its effect on flow in arterial conduits. Int. J. Numer. Meth. Fluid. **57**(5), 495–517 (2008)
9. Gambaruto, A.M., Janela, J., Moura, A., Sequeira, A.: Sensitivity of hemodynamics in patient specific cerebral aneurysms to vascular geometry and blood rheology. Math. Biosci. Eng. **8**(2), 409–423 (2011)
10. Goljan, E.F.: Rapid Review Pathology. Mosby/Elsevier, Philadelphia (2010)
11. Hassan, T., Timofeev, E.V., Saito, T., Shimizu, H., Ezura, M., Matsumoto, Y., Takayama, K., Tominaga, T., Takahashi, A.: A proposed parent vessel geometry based categorization of saccular intracranial aneurysms: Computational flow dynamics analysis of the risk factors for lesion rupture. J. Neurosurg. Pediatr. **103**(4) (2005)
12. Heywood, J.G., Rannacher, R., Turek, S.: Artificial boundaries and flux and pressure conditions for the incompressible Navier-Stokes equations. Int. J. Numer. Meth. Fluid. **22**(5), 325–352 (1996)
13. Janela, J., Moura, A., Sequeira, A.: Absorbing boundary conditions for a 3D non-Newtonian fluid–structure interaction model for blood flow in arteries. Int. J. Eng. Sci. **48**(11), 1332–1349 (2010)
14. Krex, D., Schackert, H.K., Schackert, G.: Genesis of cerebral aneurysms–an update. Acta Neurochir. **143**(5), 429–449 (2001)
15. Ku, D.N.: Blood flow in arteries. Annu. Rev. Fluid Mech. **29**(1), 399–434 (1997)
16. Moura, A.: The geometrical multiscale modelling of the cardiovascular system: Coupling 3D and 1D FSI models. PhD thesis, Politecnico di Milano (2007)
17. Nunes, D., Ramalho, S.: 1D hyperbolic models for blood flow in arteries. Internal Report, CEMAT (2009)

18. Quarteroni, A.M., Valli, A.: Numerical Approximation of Partial Differential Equations. Springer, Berlin (2008)
19. Ramalho, S., Moura, A., Gambaruto, A.M., Sequeira, A.: Sensitivity to outflow boundary conditions and level of geometry description for a cerebral aneurysm. Int. J. Numer. Meth. Biomed. Eng. **28**(6-7), 697–713 (2012)
20. Rinkel, G.J.E., Djibuti, M., Algra, A., Van Gijn, J.: Prevalence and risk of rupture of intracranial aneurysms: A systematic review. Stroke **29**(1), 251 (1998)
21. Robertson, A.M.: Review of Relevant Continuum Mechanics. In: Galdi, G.P., Rannacher, R., Robertson, A.M., Turek, S. (eds.) Hemodynamical Flows: Modeling, Analysis and Simulation, pp. 1–62. Birkhäuser, Boston (2008)
22. Robertson, A.M., Sequeira, A., Kameneva, M.V.: Hemorheology. In Galdi, G.P., Rannacher, R., Robertson, A.M., Turek, S., editors, Hemodynamical Flows: Modeling, Analysis and Simulation, pages 63–120. Birkhäuser, Boston (2008)
23. Sazonov, I., Yeo, S.Y., Bevan, R.L.T., Xie, X., van Loon, R., Nithiarasu, P.: Modelling pipeline for subject-specific arterial blood flow - a review. Int. J. Numer. Meth. Biomed. Eng. (2011) DOI: 10.1002/cnm.1446.
24. Sequeira, A., Janela, J.: An overview of some mathematical models of blood rheology. In: Pereira, M.S. (ed.) A Portrait of Research at the Technical University of Lisbon, pp. 65–87. Springer, Berlin (2007)
25. Sequeira, A., Moura, A., Janela, J.: Towards a geometrical multiscale approach to non-Newtonian blood flow simulations. In: Sequeira, A., Rannacher, R. (eds.) Advances in Mathematical Fluid Mechanics - dedicated to G.P. Galdi on his 60th birthday, chapter 295–309. Springer, Berlin (2009)
26. Sezgin, M., Sankur, B.: Survey over image thresholding techniques and quantitative performance evaluation. J. Electron. Imag. **13**(1), 146–165 (2004)
27. Tu, C., Deville, M.: Pulsatile flow of non-Newtonian fluids through arterial stenosis. J. Biomech. **29**(7), 899–908 (1996)
28. Wulandana, R., Robertson, A.M.: An inelastic multi-mechanism constitutive equation for cerebral arterial tissue. Biomech. Model. Mechanobiol. **4**(4), 235–248 (2005)